Effect of heat treatment on the microstructure and magnetic properties of laser powder bed fusion processed equiatomic Co-Fe

Liogas, Konstantinos; Lau, Kwang Boon; Wang, Zifan; Brown, David; Polatidis, Efthymios; Wang, Pei; Korsunski, Alexander

DOI:
10.1016/j.addma.2023.103499

Additive Manufacturing 67 (2023) 103499

Contents lists available at ScienceDirect

Additive Manufacturing

journal homepage: www.elsevier.com/locate/addma

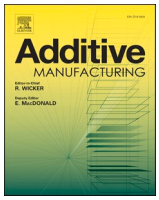

Effect of heat treatment on the microstructure and magnetic properties of laser powder bed fusion processed equiatomic Co-Fe

Konstantinos A. Liogas [a,b,*], Kwang Boon Lau [b], Zifan Wang [c], David N. Brown [d], Efthymios Polatidis [e], Pei Wang [b,f], Alexander M. Korsunsky [a,*]

[a] MBLEM, Department of Engineering Science, University of Oxford, Parks Road, Oxford OX1 3PJ, United Kingdom
[b] Institute of Materials Research and Engineering, Agency for Science, Technology and Research, 2 Fusionopolis Way, Singapore 138634, Republic of Singapore
[c] Department of Engineering, University of Cambridge, Trumpington Street, Cambridge CB2 1PZ, United Kingdom
[d] School of Metallurgy and Materials, University of Birmingham, Edgbaston B15 2TT, United Kingdom
[e] Paul Scherrer Institute, Laboratory for Neutron Scattering and Imaging (LNS), Villigen 5232, Switzerland
[f] Engineering Cluster, Singapore Institute of Technology, 10 Dover Drive, Singapore 519961, Republic of Singapore

A B S T R A C T

Equiatomic Cobalt-Iron (Co-Fe 50%at.) has great potential as a soft magnetic alloy, but its wider use has been limited by its poor workability and strength. Recent advancements in Laser Powder Bed Fusion (LPBF), an Additive Manufacturing (AM) technique, provided a new pathway for constructing fully dense, structurally sound, complex-shaped components from bulk equiatomic Co-Fe in a single process step. To obtain the desirable soft magnetic performance in the alloy, thermal post-processing with a controlled slow cooling needs to be applied. In order to identify the optimum heating conditions, several single and multiple step heat treatment profiles were performed and compared. The effects of the thermal post-processing on the microstructure, structural ordering, and functional properties of the alloy after each heat treatment were investigated using electron microscopy, neutron diffraction (ND), electron backscatter diffraction (EBSD), and quasi-static magnetic characterisation in a closed loop magnetic circuit. Results have shown that a normalisation heat treatment at 1300 K for 2-hours followed by a 4-hour primary heat treatment at 1123 K and slow cooling to room temperature produced a recrystallised microstructure characterised by predominantly equiaxed grains with an average size of up to 61 μm, and a fully ordered B2 structure. The quasi-static soft magnetic properties obtained were favourable compared to those of commercial Co-Fe grades, with maximum relative permeability higher than 8000, coercivity as low as 112 A/m and magnetic saturation polarization of 2.39 Tesla. These findings provide the basis to enable the manufacturing of three-dimensional complex-shaped electromagnetic cores by LPBF.

1. Introduction

Co-Fe (Cobalt-Iron) intermetallic compounds are industrially important soft magnetic alloys that possess high saturation induction (B_s), high Curie temperatures (T_c), as well as good maximum relative permeability (μ_{max}) and coercivity (H_c) [1]. They are ideal candidates for extreme temperature applications such as aerospace generators, starter motors and high flux electromagnetic circuits [2,3]. Co-Fe systems are particularly interesting since $Co_{(1-x)}Fe_x$ alloys with x = 30–70 at%, undergo an order – disorder transformation above 1000 K [4]. At these elevated temperatures Co and Fe are distributed randomly on the sites of a body-centred cubic (BCC) lattice. Below the order – disorder transformation temperature Co and Fe atoms are arranged into two interpenetrating primitive cubic sublattices and form an ordered B2 (CsCl) structure [4]. It has been shown that the ordered and disordered phases exhibit significantly different functional and structural properties [5].

The highest possible saturation induction at room temperature of 2.45 T (Tesla) was first identified by Preuss and Weiss in the composition Co_{35}-Fe_{65} [6,7]. Later, Ellis and Elmen discovered that the almost equiatomic alloy (50 at% Co) had higher maximum relative permeability of around ~8000 and a saturation induction of 2.40 T [8–10]. However, the equiatomic Co-Fe alloy exhibits extremely brittle mechanical behaviour and this hampers the fabrication of bulk electromagnetic components by conventional manufacturing (CM) routes such as casting, forging, and rolling [5,11,12]. The brittleness of equiatomic Co-Fe was attributed to the formation of the ordered B2 phase [5,11,12].

Recent advancements in laser-based Additive Manufacturing (AM) provided a new pathway for constructing complex-shaped electromagnetic components from bulk equiatomic Co-Fe in an efficient, net-shaping single process [14–16]. In addition, the properties of AM-fabricated components such as structural ordering, precipitate

* Corresponding authors at: MBLEM, Department of Engineering Science, University of Oxford, Parks Road, Oxford OX1 3PJ, United Kingdom.
E-mail addresses: konstantinos.liogas@stcatz.ox.ac.uk (K.A. Liogas), desmond_lau@imre.a-star.edu.sg (K.B. Lau), zw421@cam.ac.uk (Z. Wang), d.brown.5@bham.ac.uk (D.N. Brown), efthymios.polatidis@psi.ch (E. Polatidis), wangp@imre.a-star.edu.sg (P. Wang), alexander.korsunsky@eng.ox.ac.uk (A.M. Korsunsky).

https://doi.org/10.1016/j.addma.2023.103499
Received 20 December 2022; Received in revised form 19 February 2023; Accepted 13 March 2023
Available online 15 March 2023

formation, and texturing can be fine-tuned by changing the process parameters to suit the particular set of required material characteristics [13,14,17,18]. Previous studies have demonstrated that the high cooling rates ($>10^3$ K/s) associated with the Laser Powder Bed Fusion (LPBF) technique can suppress the formation of the brittle B2 phase and induce a BCC ductile phase [14,15]. However, the disordered BCC cannot be fully realised as previous detailed studies revealed small portions of B2 ordered phase in AM processed Co-Fe samples [14,15]. Ordering has been demonstrated that can be varied based on sample size and cooling rates in different AM methods [14,15,20]. Even so, it has been reported that LPBF AM technique, can produce as-fabricated (AF) equiatomic Co-Fe samples that yield a ductility of $\approx 13 - 30\%$ accompanied by strength of ≈ 700 MPa [15,16]. However, even though good mechanical properties were obtained, these previous studies didn't managed to match the soft magnetic performance of AM Co-Fe to that of conventionally manufactured Co-Fe used in electrical machines, actuators and high-performance transformers [5,10,11,19,21].

Fundamentally, the magnetic properties of bulk Co-Fe alloys are strongly dependent on the microstructure as well as structural ordering [22,23]. For instance, the shape of magnetic hysteresis loop, coercivity and relative permeability are determined both by the intrinsic material properties such as magneto-crystalline anisotropy and magnetostriction constants, as well as microstructural characteristics like grain size, crystallographic defects, crystallographic texture, and precipitates [5, 11,19]. Structural ordering is also known to affect the average magnetic moment per atom [24–27], as well as the spatial arrangement of atoms and the lattice constant. Furthermore, the arrangement of atoms in Co-Fe can affect the magneto-crystalline anisotropy [23]. Magnetic properties such as coercivity and initial permeability in a soft magnetic material can be described as functions of average grain size (D), magneto-crystalline anisotropy, and lattice parameter, based on the Grain Size Dependence of Coercivity and Permeability (GSDCP) theory [28–33]. Therefore, promoting a softer magnetic behaviour in the Co-Fe requires obtaining low magneto-crystalline anisotropy and higher lattice constant by increasing the structural ordering [19,20,24–27], together with defect-free large equiaxed grains [22,33]. The aforementioned characteristics can be obtained by choosing the most appropriate manufacturing methods together with appropriate thermal post-processing treatments to achieve the optimum functional and structural properties [5,11]. These considerations motivated the work reported in this paper to characterise the effects of thermal post-processing on the microstructure, structural ordering, and soft magnetic properties of LPBF equiatomic Co-Fe. The observed functional property relationships are interpreted by considering the alloy microstructure and ordering in each specific manufactured and thermally post-processed condition.

2. Materials and methods

The powder used in this study was a pre-alloyed gas-atomised equiatomic Co-Fe powder supplied by Sandvik AB, Sweden. The particle cross-section morphology (Fig. 1(a-b)) was imaged by Scanning Electron Microscopy (SEM) using LYRA3 dual-beam FIB-SEM microscope located in the Oxford Multi-Beam Laboratory for Engineering Microscopy (MBLEM) (TESCAN Orsay Holding, Brno, Czech Republic) with a 20 kV accelerating voltage and a working distance of 9 mm. Micrographs were recorded using Secondary Electron (SE) and Backscattered Secondary Electron (BSE) detection modes. One powder sample was simply mounted on a carbon tape to show the particle morphology, whilst the second was polished to show the particles cross-section, Fig. 1(a -b). Particle size distribution was measured with a Malvern 2000 laser diffraction analyser by Malvern Panalytical Ltd, Malvern, UK. The

Table 1
Summary of particle size data for Co-Fe powder.

Average	Co-Fe Powder
D_{10} (μm)	18.1
D_{50} (μm)	32.4
D_{90} (μm)	56.4

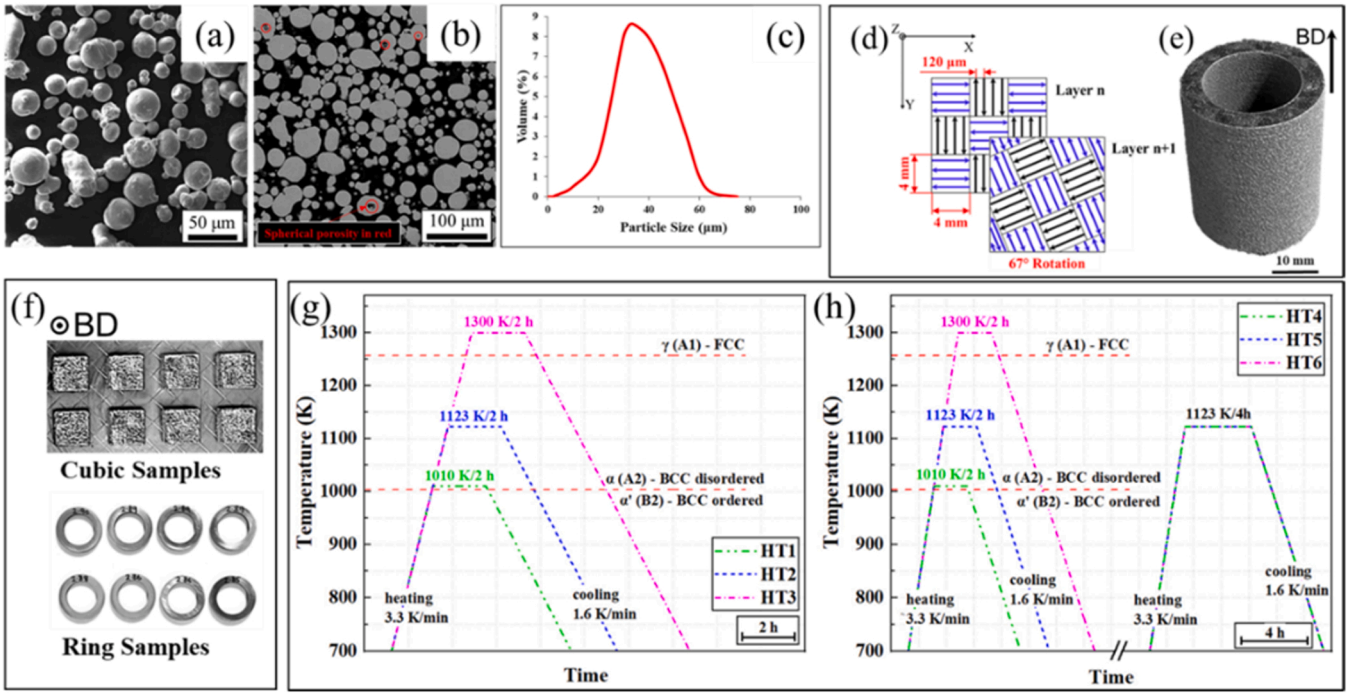

Fig. 1. (a-c) SEM micrographs showing (a) powder morphology, (b) ground and polished to reveal porosity, (c) a graph of the powder size distribution. (d) Schematic representation of the chessboard island scanning strategy. The black and blue arrows represent the scan vectors within each of the island with the distance between these vectors defined as the scan spacing. (e) Ring-shaped AF Co-Fe samples. (f) Cubic and Ring-shaped specimens. (g-h) Heat treatment profiles with normalisation and primary heat treatments of additively manufactured Co-Fe.

results are presented in Table 1 and Fig. 1c.

To identify the composition of the as-received powder, X-ray Fluorescence Spectroscopy (XFS) was employed using a M4 TORNADO (Bruker Corporation, Billerica, Massachusetts, USA). The results are presented in Table 2. Before use the powder was first dried at 333 K for 12 h in an oven operated under vacuum to remove any adsorbed moisture.

LPBF samples were fabricated using a TruPrint 1000 system (TRUMPF GmbH, Ditzingen, Germany) that utilised a 200 W (1070 nm) YLR-Faser-Laser and allowed the laser spot to scan the surface of the powder bed at a maximum speed of 7000 mm/s. TruPrint 1000 used a fixed laser spot size of 30 μm and has a maximum build plate diameter of 100 mm and buildable height of 98 mm. The building plate made from austenitic stainless steel 316 L was not preheated during operation to ensure high cooling rates, therefore causing the formation of disordered BCC phase in the AF Co-Fe samples. 3D printing of the specimens was performed under argon (Ar) atmosphere (purity: 99.9995%) to prevent oxidation, and the O_2 content in the chamber was reduced down to ~100 ppm. Gas pressure within the chamber was kept at 5 bar during printing. A parametric study was conducted by varying hatch spacing (h) and scanning speed (u). The laser power (P) and layer thickness (t) were kept constant. The LPBF machine was located in the Insitute of Materials Research and Engineering (IMRE), Singapore.

A CUT P 800 Electron Discharge Machine (EDM) (Georg Fischer AG, Schaffhausen, Switzerland) was used to extract the following sample sets: 10 × 10 × 10 mm cubic samples for metallographic analysis (Fig. 1 f); a bar sample with the diameter of 6 mm and height of 10 mm for Neutron Diffraction (ND) measurements; ring samples with a height of 2 mm, an outer diameter of 29 mm, and an inner diameter of 20 mm for quasi-static magnetic characterisation (Fig. 1 f).

The ring and cubic specimens were heat-treated in an STF 16/450 tube furnace (Carbolite Gero Ltd, Sheffield, UK) under Ar atmosphere. The different thermal profiles used in this study are presented in Table 3 and Fig. 1(g-h). Ramp-up rate was kept at 3.3 K/min for all heat treatments. Holding time at the different target temperatures was 2 h for the normalisation heat treatment with a cooling rate of 1.6 K/min. Similar heating rates were used for the primary heat treatment with a holding time of 4 h and fixed cooling rate of 1.6 K/min. Samples were allowed to cool down to 400 K, after which they were left to cool down to room temperature in the furnace. The primary heat treatment profile was kept identical in all cases as it was designed based on ASTM A801 thermal post-process standards for wrought Co-Fe alloys [34,35].

For the metallographic analysis, AF and heat-treated (HTs) cubic samples were hot-pressed mounted and ground with 400, 800 and 1200 grit grinding papers, followed by fine mechanical polishing in a water-based solution containing suspensions of 9 μm, 3 μm and 1 μm diamond particles. Eventually a 0.1 μm colloidal silica by Struers GmbH was used as the finishing step. SEM imaging was performed in MBLEM using the TESCAN LYRA3 dual-beam FIB-SEM microscope at 20 kV accelerating voltage and a working distance of 9 mm. Micrographs were collected in the BSE mode, and Electron Backscatter Diffraction (EBSD) mapping was carried out using the integrated SYMMETRY detector (Oxford Instruments, Abingdon, Oxfordshire, UK). EBSD maps covered the area of 1 mm × 1 mm with an acquisition step size of 0.64 μm. All the acquired EBSD data were post-processed by MATLAB using MTEX texture and crystallographic analysis toolbox [36].

Samples for Transmission Electron Microscopy (TEM) were prepared using the Focused Ion Beam (FIB) lift-out method using FEI Helios NanoLab 450 S (Thermo Fisher Scientific, USA). Specimens prepared using FIB were thinned to approximately 100 nm using the accelerating voltage of 30 kV and current of 80 pA. An Ar ion plasma with an energy of 5 kV was employed for the final polishing and removal of any FIB-induced damage. TEM analyses were conducted in the TEM/STEM mode using FEI Titan 300 microscope (Thermo Fisher Scientific, USA).

Table 2
Chemical composition of the investigated Co-Fe alloy (at%).

Element	Fe	Co	Si	O	C	P
Content (at%)	Bal.	49.30	0.02	0.43	0.05	0.01

Table 3
Details of Heat Treatment Profiles.

Sample code	Normalisation heat treatment	Primary heat treatment
AF (as-fabricated)	–	–
HT1	1010 K / 2 h	–
HT2	1123 K / 2 h	–
HT3	1300 K / 2 h	–
HT4	1010 K / 2 h	1123 K / 4 h
HT5	1123 K / 2 h	1123 K / 4 h
HT6	1300 K / 2 h	1123 K / 4 h

Neutron diffraction (ND) measurements were performed using the time-of-flight POLDI diffractometer in the Swiss Spallation Source, at Paul Scherrer Institute (PSI, Switzerland). POLDI instrument has one detector bank at the scattering angle of 90° relative to the incident neutron beam. Bar samples were aligned with their long dimension parallel to the scattering vector. The neutron diffraction data were reduced and fitted using the open-source software Mantid [37].

Quasi-static magnetic properties were characterised using the closed-circuit methods under Direct Current (DC) [38–40]. The magnetic characterisation setup used in this experiment for measuring the initial magnetisation curves and hysteresis loops was designed and calibrated in accordance with the ASTM A773 standards by the first author [39]. Before any measurement the samples were strictly demagnetised according to the standards [39]. Flux density (B [T]) versus magnetic field strength (H [A/m]) initial magnetisation curves derived by the ring samples, were used to measure the maximum relative permeability (μ_{max}), and flux density value at a field strength of 5000 A/m (B_{5000} [T]). Remanence (B_r [T]) and coercivity (H_c [A/m]) for every sample were derived from the quasi-static B-H hysteresis loops of each specimen. All the magnetic measurements on the ring samples were conducted with primary winding of 43 turns, secondary winding of 20 turns, and maximum primary winding current of 12 Amps. The magnetic flux was set to be perpendicular to the build direction during magnetic measurements for all samples. For the measurement of saturation polarization values J_{sat} [T] (J = B - μH), J-H curves were obtained from the cubic-shaped samples with a PERMAGRAPH®-L hysteresis graph system (MAGNET-PHYSIK, Dr. Steingroever GmbH, Köln, Germany) [41]. This magnetic characterisation machine was designed and calibrated in accordance with the ASTM A977/A977M standards [40]. All the magnetic measurements were conducted at temperature of 293 K and relative humidity of 40%.

3. Results and discussion

3.1. As-fabricated microstructure of Co-Fe

To identify the optimum printing parameters that yield low porosity and crack-free equiatomic Co-Fe samples, a parametric study was conducted by varying scanning speeds (u = 300 mm/s – 1100 mm/s), and hatch spacings (h = 30–150 μm). At the same time, the laser power, and layer thickness were kept constant at P = 120 W, and t = 20 μm respectively. During printing a chessboard scanning strategy was used for all samples with an island size of 4 × 4 mm^2 and 67° rotation of the laser scanning direction between successive layers, Fig. 1(d). Micrographs of the twenty-five different combinations of parameters are presented on Fig. 2(a-y) and results of mean porosity (%) on Fig. 2(z). The builds were characterised to assess the degree of consolidation and the impact of the process parameters. Since a fixed layer thickness of 20 μm and laser powder of 120 W were used for all the samples, a three-dimensional energy density factor from Eq. (1), representing the key

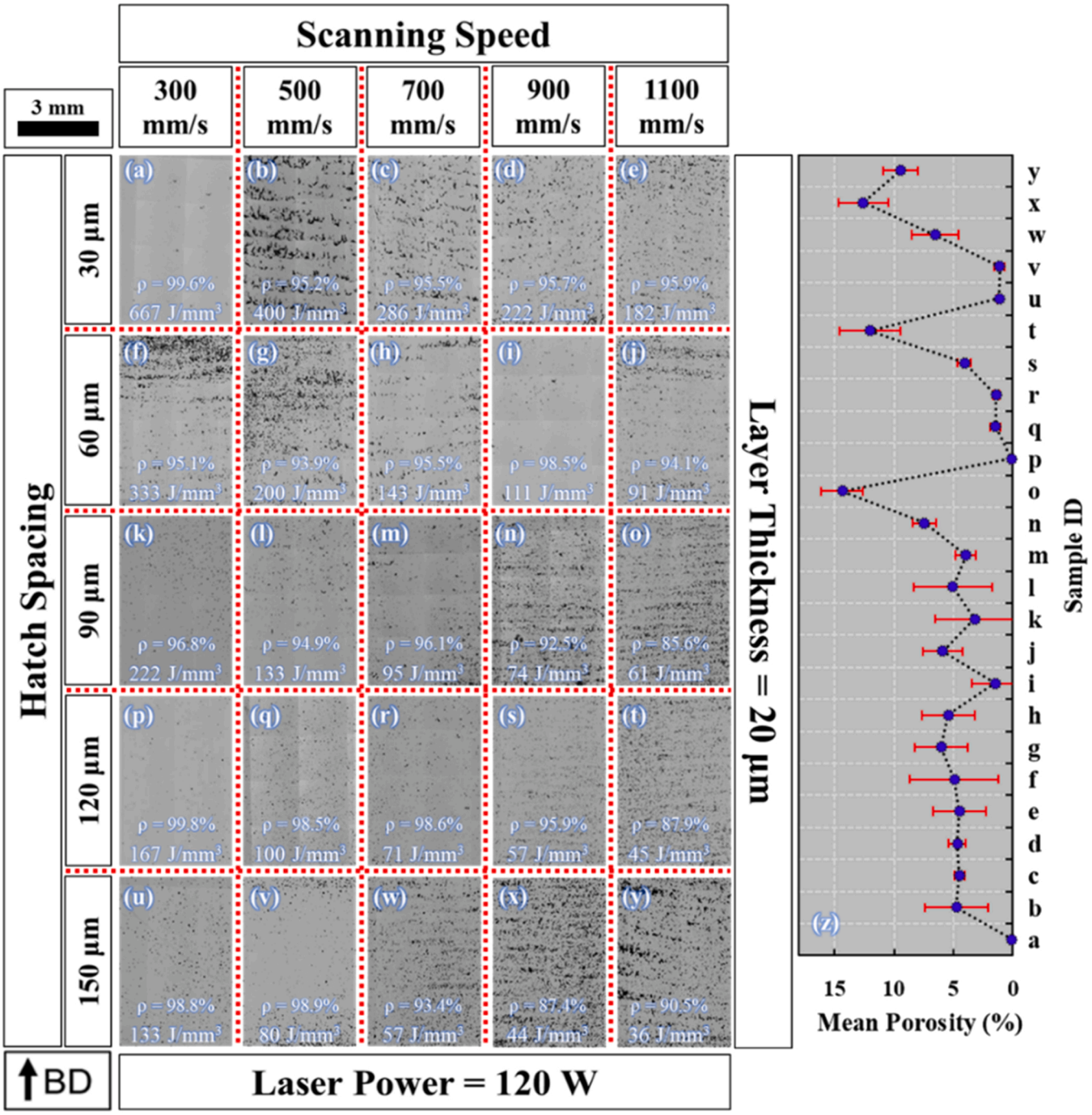

Fig. 2. Representative micrographs showing the influence of LPBF process parameters on the consolidation behaviour in the equiatomic Co-Fe.

process variables to give a semi-quantitative estimate of the heat input [42] was chosen to identify the heat input threshold required to achieve maximum consolidation and minimum porosity or cracks. Build conditions with E< 89 J/mm^3 displayed the highest porosity percentages. A sharp decrease of porosity was observed when scanning speed of 300 mm/s was used (a, f, k, p, u). From these results the highest relative density was observed in the sample (p). Therefore, the optimum printing parameters used to manufacture the rest of the samples where: layer thickness of 20 µm, laser power of 120 W, scan speed of 300 mm/s, and hatch spacing of 120 µm. Based on the classical definition on Eq. (1), volumetric energy density was calculated to be around ~167 J/mm^3. All build parameters presented in Table 3. No cracks were observed in any of the samples, even in the ones with relatively high porosity.

$$E\left(\mathrm{J}\Big/\mathrm{mm}^3\right) = P(\mathrm{W})\Big/\left[h(\mu\mathrm{m}) \bullet u\left(\frac{\mathrm{mm}}{\mathrm{s}}\right) \bullet t(\mu\mathrm{m})\right] \quad (1)$$

These printing parameters presented on Table 4, produced crack-free, highly dense (around ~99.8 ± 0.05%) samples.

Fig. 3(a) shows the grain morphology of the AF Co-Fe sample with the build direction (BD) vertical in all images as indicated by the black arrow.

The BSE image and EBSD map in Fig. 3(a) reveal a hybrid microstructure consisting of fine elongated grains along with regions of smaller equiaxed grains. The relatively fine grain size is a consequence of the high cooling rate inherent to the LPBF process [43]. TEM imaging elucidated the substructure composed of tangled dislocation networks, see Fig. 3(b), with occasional nanoscale voids/pores, see Fig. 3(c),

Table 4
LPBF processing parameters.

Parameters	Value
Laser Power	120 W
Scanning Speed	300 mm/s
Hatch Spacing	120 μm
Rotation Between Layers	67°
Layer Thickness	20 μm
Scanning Strategy	Chessboard
Island Size	4×4 mm^2
Energy Density	167 J/mm^3

consistent with previous studies [15]. Coupled STEM/EDS imaging conducted previously by members of our group [15], revealed dispersed silica particles with diameter of 60–90 nm located at the grain-boundaries and within grains. Additionally it has been shown that Co and Fe were distributed uniformly without any signs of segregation [14,15]. A small amount of Si was intentionally added to the Co-Fe before its atomisation to decrease the melting point and increase the melt flowability, both of which facilitated better gas-atomisation for powder manufacturing subsequently. As Si addition was indispensable, control of the oxygen content during printing and HT is vital.

3.2. Effect of heat treatment on microstructure

EBSD maps in Fig. 4(a-h) show the crystallographic texture of grains in the vertical (along BD) and horizontal directions. Pole figures reveal the preferred orientations of the $<100>$, $<110>$, and $<111>$ crystallographic directions with respect to the sample axes. The AF condition in Fig. 4(a) was found to have the average grain size of ~10.3 μm and a near random crystallographic texture with the maximum intensity = 1.7 MRD (multiples of a random distribution). HT1 condition following the normalisation heat treatment at 1010 K for 2 h, see Fig. 4(b), resulted in insufficient grain growth with the average grain size of ~10.9 μm and random crystallographic texture. HT2 at 1123 K for 2 h, see Fig. 4(c), induced a bimodal grain structure consisting of the combination of very small and large grains, indicating that some abnormal grain growth took place during that heat treatment. The small grains had a diameter of only a few micrometres, whereas some of the largest grains had a diameter of over 200 μm, resulting in the average grain size for HT2 of ~29 μm. This implies that some of the grain boundaries could be pinned by the second phase silica particles that did not dissolve during heat treatment, as it has been suggested and investigated by previous studies [14–16]. Some grain growth was not impeded due to pinning effects being overcome due to local grain orientation and misorientation across adjacent grains [44,45]. HT3 involved normalisation heat treatment at 1300 K for 2 h, see Fig. 4(d), and resulted in a larger number of big equiaxed grains, along with an area of smaller grains. The average grain size was found to be 46 μm. In HT3 the largest grains were equiaxed and presented sizes up to 130 μm, while smaller grains with sizes below 30 μm were also present. This suggested that the recrystallisation process was not fully completed. The EBSD analysis in Fig. 4(e-f) indicates that the normalisation and primary heat treatments HT4 and HT5 were also unable to introduce a fully recrystallised structure. Their respective average grain sizes, morphologies, and textures were very similar and almost identical to those of HT2. Slightly larger grains were observed in HT5 due its longer exposure to higher temperatures. EBSD maps in Fig. 4(g-h) show the HT6 microstructure in the vertical (BD) and horizontal directions, respectively. HT6 consisted of the normalisation step at 1300 K for 2 h followed by a 4 h primary heat treatment at 1123 K, and resulted in an equiaxed structure with relatively large grain size seen both in the vertical and horizontal directions with respect to the BD. The average grain size of HT6 was found to be ~61 μm. This outcome of increasing the normalisation heat treatment maximum temperature above the austenitic transformation of equiatomic Co-Fe [4] suggested that residual stresses and microstructural obstacles hindering grain-growth inherited from the process were overcame. It is concluded that a longer primary heat treatment allows the specimen to be completely recrystallised.

3.3. Neutron diffraction study

Neutron diffraction was used to determine the structural ordering of AF, HT3, and HT6 states, Fig. 5. Neutron diffraction was used to determine the degree of ordering, since X-ray scattering factors of the constituent elements, Co and Fe, are nearly equal and therefore the superlattice diffraction peaks are very weak [46–48]. It was proven that the ordering parameter was dependent on the cooling rate and only slightly changed with the holding time. The relevant crystallographic planes indicated. Neutron diffraction peaks were used to derive the relative degree of atomic ordering by identifying the integrated intensity ratio of the superlattice reflection peak (I_{210}) to the fundamental peak (I_{211}). These ratios were normalised to the HT6 heat treatment following the Eq. 2 from [14,46–48] taking S/S_{HT6} as the ratio of ordering with respect to the HT6 heat-treated condition.

$$\frac{S}{S_{HT6}} = \sqrt{\frac{\frac{I_{210}}{I_{211}}}{\left(\frac{I_{210}}{I_{211}}\right)_{HT6}}} \tag{2}$$

The HT6 conditions was selected as normalisation point due to the complete remove of residual stresses and the promotion of complete recrystallisation, while the slow cooling allowed sufficient time for the complete ordering transformation to take place. The relative ordering values were calculated to be ~0, 0.98, 0.99 for AF state, HT3 and HT6 states, respectively. According to the phase diagram of the equiatomic Co-Fe, disordered BCC phases is thermodynamically stable above 1000 K [5,11]. On the other hand, HT3, and HT6 states were characterised by a fully ordered B2 (CsCl) phase due to their slow cooling rate to room temperature. High values of relative ordering have been reported from previous studies in the Co-Fe kinetics using neutron diffraction as well as TEM microscopy after a heat treatment with a slow cooling [14,46–48].

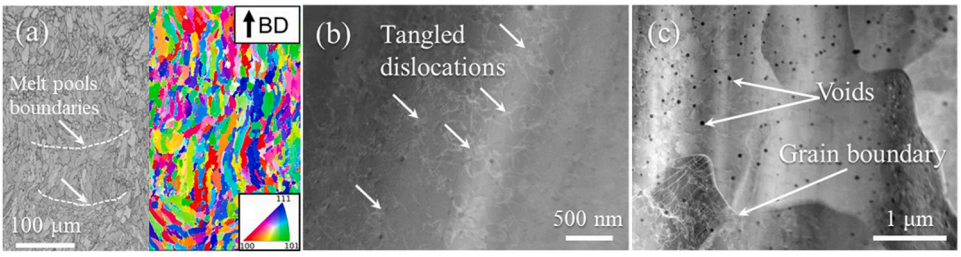

Fig. 3. Representative TEM and STEM images of AF Co-Fe: (a) BSE and EBSD images of AF Co-Fe. Melt pool boundaries are indicated using white dashed curves. (b), and (c) TEM images of dense and tangled dislocations as well as voids in AF Co-Fe..

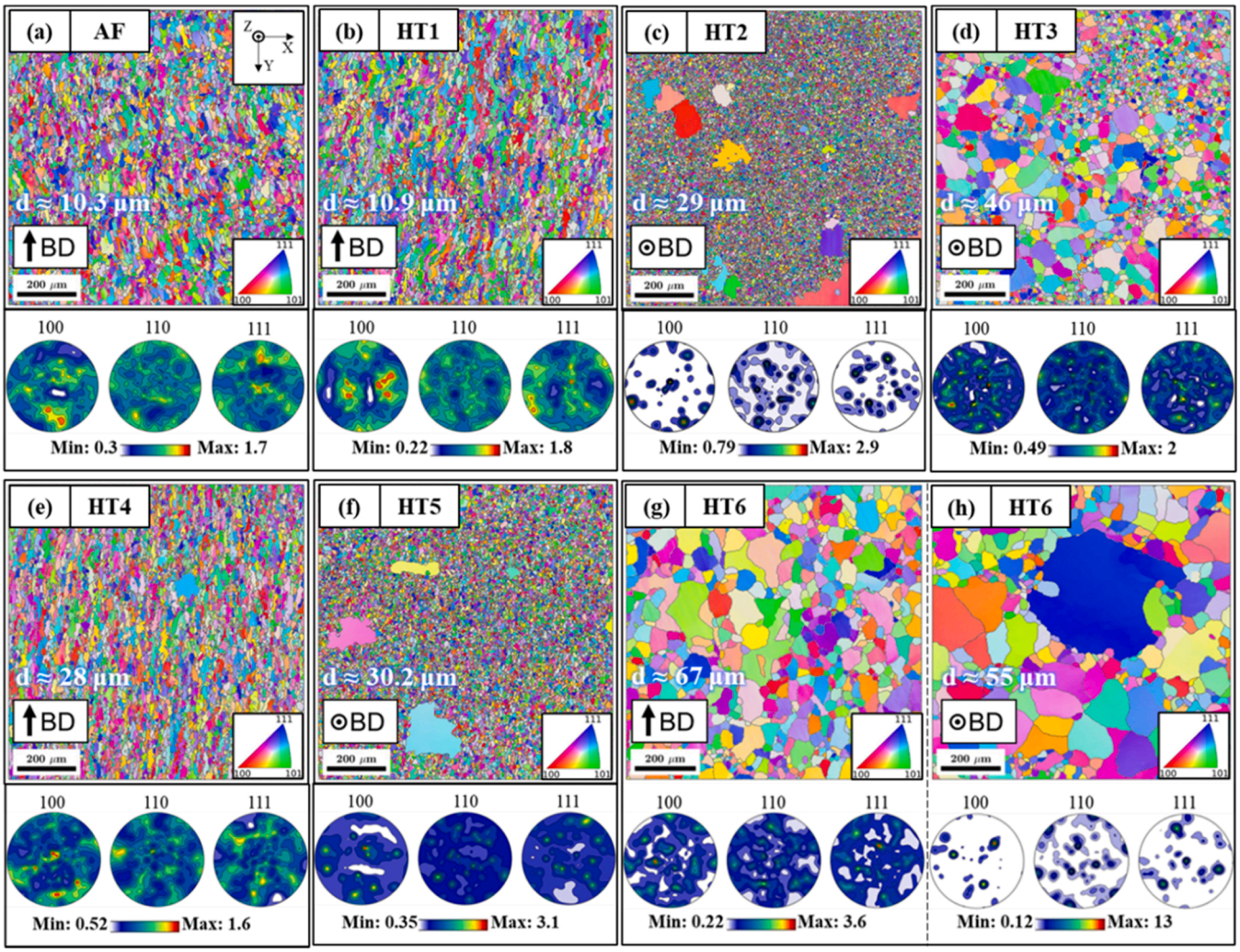

Fig. 4. EBSD maps and pole figures (PFs) for AF and all heat-treated (HT) conditions. The top images in every box correspond to EBSD maps taken vertically or horizontally with respect to the building direction (BD), while the bottom boxes are PFs showing the preferred orientation of the $< 100 >$, $< 110 >$ and $< 111 >$ crystallographic directions with respect to the sample axes direction for every condition.

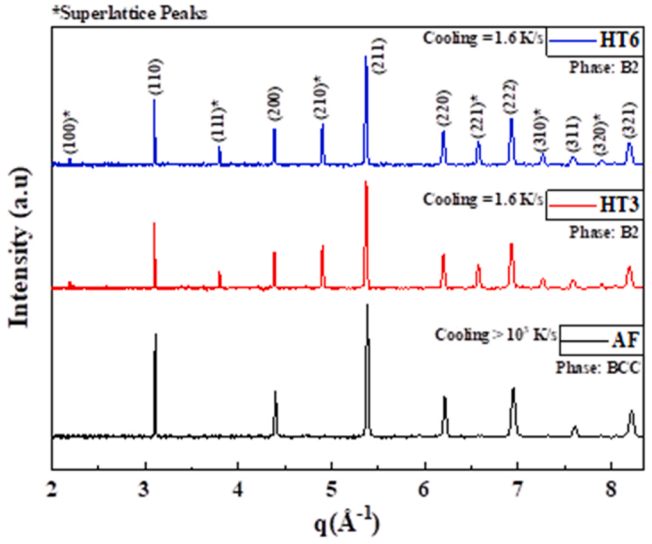

Fig. 5. Neutron diffraction patterns for AF, HT3 and HT6 samples. AF sate is a fully disordered BCC, while HT3 and HT6 after slow cooling exhibit an ordered B2 structure.

3.4. Quasi-static soft magnetic properties

The quasi-static magnetic characterisation was performed on the AF and heat-treated ring and cubic-shaped specimens. The B-H hysteresis loops, B-H initial magnetisation and μ_{max} curves are shown in Fig. 6(a-f). The magnetic properties such as the value of the flux density at magnetic field strength of 5000 A/m (B_{5000}), coercivity (H_c), value of maximum relative permeability (μ_{max}), and remanence (B_r) were extracted from the plots and are listed in Table 5. alongside previously reported research results from CM and AM Co-Fe alloys. Furthermore, the evolution plots of coercivity H_c and maximum relative permeability μ_{max} in each processing condition are presented in Fig. 6(g-h), respectively. The J-H curves for studying the saturation polarization are shown in Fig. 7. Saturation Polarization (J_{sat}) and their respective magnetic field strength values (H_{sat}) are displayed in Table 6. These graphs illustrate the outstanding soft magnetic properties that can be achieved in the LPBF equiatomic Co-Fe alloy through an optimised heat treatment route. For additional comparison, the magnetic values of coercivity and maximum relative permeability of commercial Co-Fe alloys: HIPERCO® 50 A [49] and VACOFLUX 50 [50] are also reported in Table 5 and plot against this paper's results in Fig. 6(g-h).

From the quasi-static magnetic characterisation, it is evident that the equiatomic AF Co-Fe behaved as a "semi-hard" magnet with a high coercivity value of $H_c \approx 1394$ A/m, low maximum relative permeability

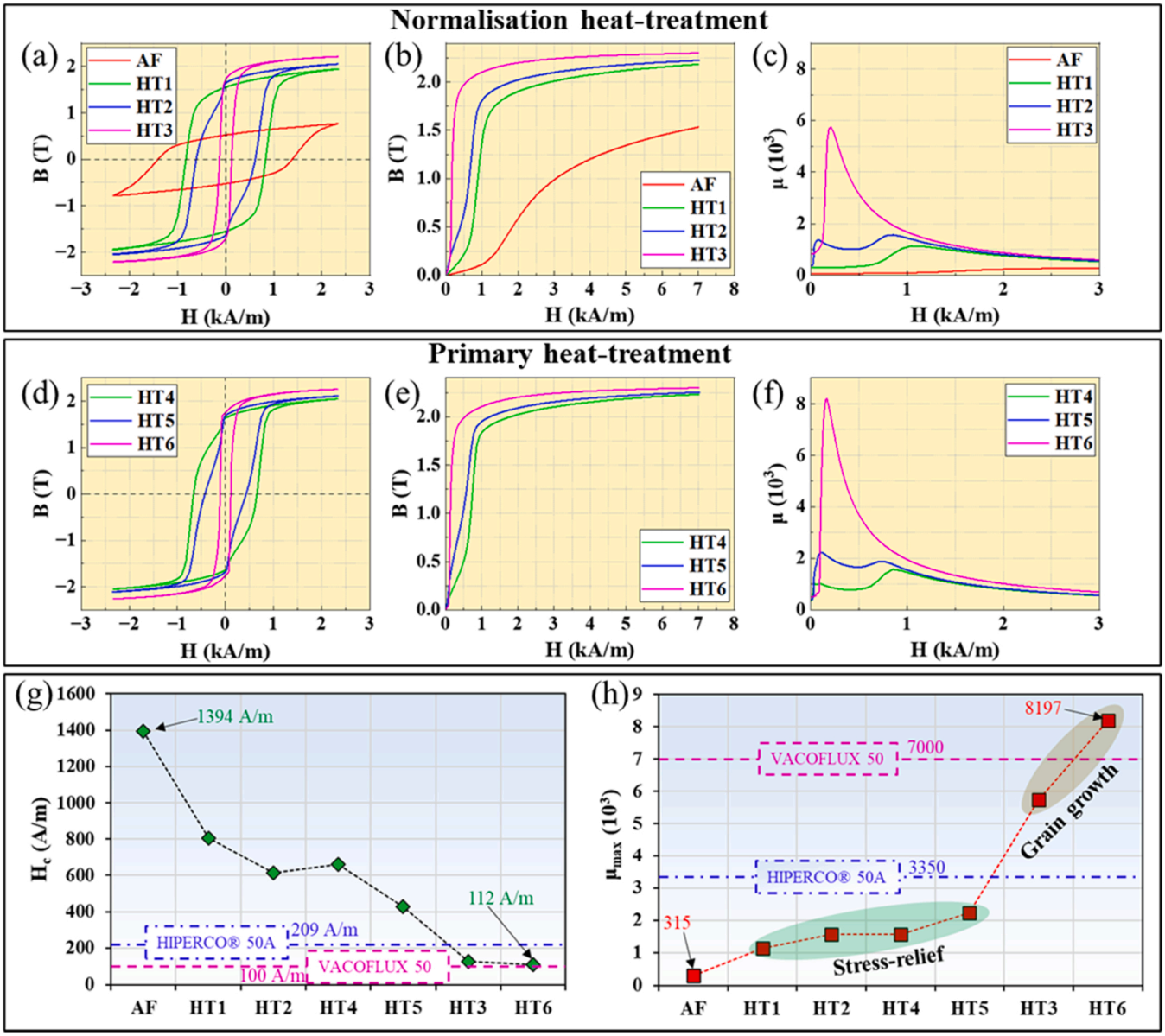

Fig. 6. Magnetic properties of Co-Fe alloy in AF, and all the different heat-treated conditions. (a-c) Results from the normalisation heat treatment, quasi-static BH hysteresis loops. (d-f) Magnetic measurements for primary heat treatment. (g-h) Evolution of the coercivity H_c, and maximum relative permeability μ_{max} of LPBF equiatomic Co-Fe after all the different heat treatments. The dashed coloured lines indicate the magnetic properties of the HIPERCO® 50 A and VACOFLUX 50, from [49,50].

of $\mu_{max} \approx 314$ and remanence of $B_r \approx 0.52$ T. It also achieved relatively small flux density value of only $B_{5000} \approx 1.34$ T at 5000 A/m. The poor magnetic performance of the AF condition originates from the presence of process-inherited residual stresses, small grain size, high dislocation density, and high levels of disordering resulting from the high cooling rates during the LPBF process. Higher values of coercivity because of structural disordering were reported in CM Co-Fe alloys and it was attributed again to the small grain size and higher magneto-crystalline anisotropy associated with the disordered condition [51]. Further increase in coercivity was observed in quenched CM Co-Fe alloys due to the internal strain created by the rapid phase transformation from the austenitic phase to the BCC disordered phase [52,54]. The same phenomenon occurs during LPBF due to its inherited high cooling rates [14,15]. However, the different heat treatments considered led to the "softening" of the magnetic properties. Residual stress relief and grain growth reduced the density of lattice defects known to have a detrimental effect on the relative permeability by acting as pinning sites for the magnetic domain walls and therefore hindering their motion [11,28]. HT1 managed to relieve the process-induced residual stresses but did not lead to sufficient recrystallisation. Even though the material displayed a "softer" magnetic response, achieving coercivity of $H_c \approx 803$ A/m, remanence of $B_r \approx 1.55$ T, and maximum relative permeability of $\mu_{max} \approx 1138$, the magnetic properties did not compare well with those of CM Co-Fe alloys. Heat treatments HT2, HT4 and HT5 resulted in magnetic hysteresis plots that displayed additional inflections and reflected a duality in their permeability. This is the reflection of a bimodal grain structure in the overall magnetic behaviour due to very small grains with multiple grain boundaries impeding domain wall motion, whilst larger grains allowed easier domain wall movement. Similar to HT1, these heat treatments failed to achieve the desirable soft magnetic response. HT2 and HT4 demonstrated almost identical performance, despite the fact that HT4 included both a normalisation and primary heat treatment steps. Magnetic measurements were in the ranges of coercivity $H_c \approx 615$–659 A/m and maximum

Table 5
Magnetic properties of Co-Fe alloys fabricated via different methods.

Materials	Fabrication Method	Condition	Major Phase	μ_{max}	H_c (A/m)	B_r (T)	B_{max} (T)	Ref.
Co-Fe / Permendur	CM	Annealed[a])	B2	7900	80	1.4	2.40	[10]
Co-Fe	CM	Annealed[a])	B2	5000–8000	150	–	2.40	[5]
Co-Fe-2V	CM	Annealed[a])	B2	4000–8000	393	1.5	2.40	[19]
HIPERCO® 50 A	CM	Annealed[a])	B2	3350	209	–	2.3 **	[49]
VACOFLUX 50	CM	Annealed[a])	B2	7000	100	–	2.29 ***	[50]
Co-Fe-1.5V	LENS	AF	BCC + B2	518	995	–	2.23 ****	[14]
		Annealed[b])	B2	1639	383	–	2.30 ****	
Co-Fe-2V	LPBF	AF	–	–	–	–	1.82 ****	[16]
		Annealed[b])	–	–	–	–	1.41 ****	
		Annealed[a])	B2	673	–	–	2.17 ****	
		Annealed[a])	B2	736	–	–	2.16 ****	
Co-Fe	LPBF	AF	BCC	503	1417	–	2.09 ***	[15]
		Annealed[b])	B2	4789	702	–	2.38 ***	
		Annealed[b])	B2	5008	450	–	2.37 ***	
Co-Fe	LPBF	AF	BCC	315	1394	0.52	1.34 *	This Work
		HT1	B2	1138	803	1.55	2.12 *	
		HT2	B2	1567	615	1.64	2.21 *	
		HT3	B2	5742	126	1.71	2.27 *	
		HT4	B2	1572	659	1.64	2.12 *	
		HT5	B2	2224	429	1.68	2.22 *	
		HT6	B2	8197	112	1.75	2.28 *	

H_c = coercive field strength, μ_{max} = relative maximum permeability, B_r = remanence, B_{max} = maximum flux density .
*B_{5000}, ** B_{16000}, *** B_{20000}, **** B_{40000}
[a]) Slow Cooling Heat treatment, [b]) Quenching Heat treatment
The magnetic properties "BULK MATERIAL (BAR)" from HIPERCO® 50 A and "DC MAGNETIC PROPERTIES OF SOLID MATERIAL" from VACOFLUX 50 datasheets were used for comparison in this study [34,35].

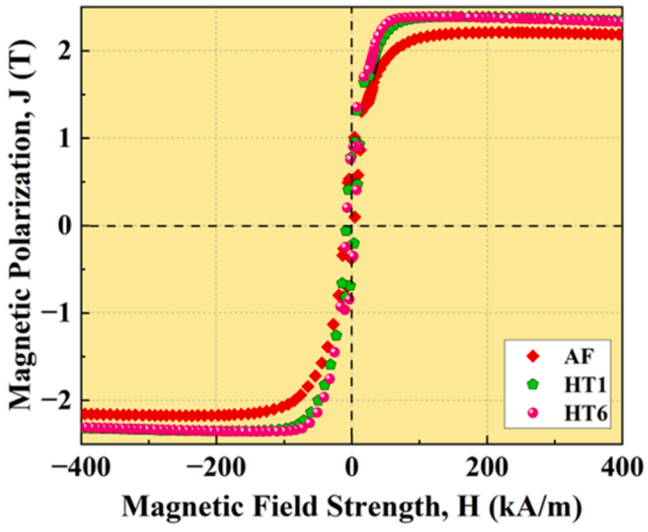

Fig. 7. Magnetic polarization J-H curves for AF, HT1, and HT6 conditions at maximum field strength of 400 kA/m.

Table 6
Saturation Polarization of LPBF Co-Fe.

Sample Code	H_{sat} (kA/m)	J_{sat} (T)
AF (as fabricated)	217	2.21
HT1	162	2.38
HT6	115	2.39

J_{sat} = Magnetic Polarization saturation value, H_{sat} = magnetic field strength value at the polarization saturation point.

relative permeability $\mu_{max} \approx 1567–1572$ for HT2 and HT4. Remanence $B_r \approx 1.64$ T was identical for both heat treatments.

HT5 showed an increase of $\mu_{max} \approx 2224$, lower $H_c \approx 429$ A/m, and slightly higher $B_r \approx 1.68$ T. The flux density at magnetic field strength of 5000 A/m were in the range $B_{5000} \approx 2.12–2.22$ T. Most of the magnetic properties obtained for AF, HT1, HT2, HT4, and HT5 are similar to those previously reported for AM processed Co-Fe alloys [14–16].

Notable improvements of soft magnetic properties were achieved after HT3 and HT6. The low values of coercivity obtained from these heat treatments led to high levels of relative permeability and flux density at lower magnetic field strength values. Larger grain size resulted in easy movement of magnetic domains, that led to the desirable softening of the alloy response. Since this resulted from increasing the normalisation heat treatment maximum temperature above the austenitic transformation of equiatomic Co-Fe [4], it is suggested that a big amount of the process-induced residual stresses as well as microstructural obstacles [51] hindering domain wall motion were overcome [14,15]. Normalisation heat treatment HT3 achieved comparable quasi-static soft magnetic performance to some CM Co-Fe alloys, with coercivity $H_c \approx 126$ A/m, maximum relative permeability $\mu_{max} \approx 5742$, and remanence of $B_r \approx 1.71$ T.

The two-step heat treatment HT6 was proven to be the optimal thermal post-processing profile for achieving ideal quasi-static soft magnetic properties directly comparable with those of the original equiatomic Co-Fe work [9,10], as well as comparing favourably with other CM Co-Fe alloys [5,11,19,20]. HT6 achieved a high value of maximum relative permeability, $\mu_{max} \approx 8197$, coercivity of $H_c \approx 112$ A/m, and remanence of $B_r \approx 1.75$ T. This heat treatment also managed to achieve higher performance of maximum relative permeability (μ_{max}) compared to both HIPERCO® 50 A [49] and VACOFLUX 50 [50] commercial Co-Fe grades. It also achieved lower coercivity value than that of HIPERCO® 50 A, $H_c \approx 209$ A/m [49]. The flux densities at 5000 A/m for HT3 and HT6 were $B_{5000} \approx 2.26–2.28$ T, respectively.

The remanence B_r, shown major improvements after different heat treatments due to the relief of process-induced residual stresses and by maintaining a level of defect density (grain boundaries, regions of smaller grains) that hinder demagnetisation [31]. In particular, B_r values of the AM equiatomic Co-Fe were higher compared to those of CM Co-Fe alloys [5,10].

The J_{sat} polarization values of single-step normalisation HT1 ~2.38 T, and two-step primary HT6 ~2.39 T heat treatments had almost identical saturation values compare to CM Co-Fe alloys [4,5,10,19] and previously studies of thermally post-processed AM Co-Fe alloys

[15]. In the AF state J_{sat} was measured to be around ~ 2.21 T. This can be attributed to the extent of chemical disordering in the AF state. It has been reported previously that disordered BCC phase possess a smaller saturation polarization compared to the ordered B2 phase in both CM and AM Co-Fe [20,22].

It is noteworthy to mention that while H_c, and μ_{max} vary over the different heat treatments, their product remains approximately constant, because both properties depend on the extent of structural ordering, grain size, stresses, and pinning forces that lattice defects exert on domain wall motion [28,51,53]. The observed higher saturation polarization J_{sat}, after the normalised and primary heat treatments can be attributed to the higher average moment per atom in the B2 structure formed after slow cooling, compared to lower average moment per atom in the disordered BCC in the AF condition [24–27]. It has also been reported by previous studies [20], that a two-step heat treatment of AM Co-Fe alloys, substantially coarsen anti-phase domains boundaries, and induces a higher degree of ordering than the one observed in single step thermal processes. Furthermore, the improvement of magnetisation at higher fields is also associated with the spatial arrangement of atoms in the ordered lattice [19,22]. Lattice constant of the ordered Co-Fe was reported to be higher, around ~ 2.851 Å compared to the disordered version of the alloy ~ 2.849 Å [19]. Additionally, the arrangement of atoms in the ordered Co-Fe alloy decreases the magneto-crystalline anisotropy, thus inducing a softer magnetic response [23]. The improvement of H_c and μ_{max} are also heavily depended on all the aforementioned factors, with the addition of grain size. Based on the GSDCP theory [29–33] H_c and initial permeability (μ_i) that correlates with μ_{max}, can be described as functions of average grain size (D). For example, by referring to the expression for coercivity in Eq 3 [22]:

$$H_c \approx 3\sqrt{\frac{k_B T_c K_1}{\alpha J_s}}\ \frac{1}{D} \tag{3}$$

Where D is the average grain size [μm], k_B is the Boltzmann's constant, T_c is the Curie temperature [K], K_1 is the magneto-crystalline anisotropy [J/cm^3], α is the lattice constant [Å], and J_{sat} is the magnetic saturation polarization [T]. With a combination of lower magneto-crystalline anisotropy, higher lattice constant and magnetic saturation polarization in the ordered B2 phase, coupled with large average grain size would result in small coercivity values. Based on GSDCP theory [33], the behaviour of permeability is inversely proportional to the H_c. Therefore, a combination of large grain size, lower magneto-crystalline anisotropy, high lattice constant and magnetic saturation polarization in the ordered B2 phase results in amore permeable material [22,33].

Furthermore, [54] developed the following empirical relationship, Eq 4, for the effect of grain size on coercivity for traditional CM Co-Fe alloys based on an extensive review of published experimental data. (Fig. 8)

$$H_c = 3.42 + 758.2D^{-1} \tag{4}$$

The correlation between H_c vs D^{-1} is derived by GSDCP theory where the D^{-1} law is used to describe coercivity in an alloy with grain size larger than the domain wall width [55,56]. The grain size, and the corresponding H_c for the HT3, and HT6 samples followed a similar behaviour, which is consistent with the reported data from CM Co-Fe [22,57]. AF, HT1, HT2, HT4 as well as previously reported AM Co-Fe [15,16], didn't follow the expression exactly probably due to smaller levels of recrystallisation, lower levels of structural ordering, and possible remnants of oxidation in the solidification structure.

The outcomes of this study indicated that the quasi-static magnetic properties of LPBF Co-Fe after different heat treatments are depended on the combination of the final degree of structural ordering, and grain size. Each of the aforementioned parameters can be tuned (from the LPBF process (structural ordering of the AF state [14]), and by thermal post-process parameters (structural ordering, grain size [15,16,19,20]).

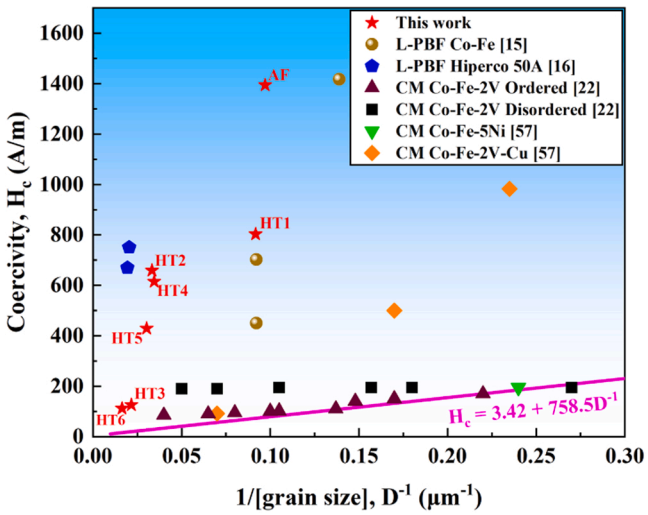

Fig. 8. Comparison of H_c vs D^{-1} for AM Co-Fe, and CM Co-Fe alloys.

4. Conclusion

In conclusion, this research study has demonstrated that highly dense equiatomic Co-Fe components manufactured via LPBF with appropriate thermal post-processing can achieve soft magnetic performance that is either comparable or better than commercially available grades.

- Parametric study revealed the optimised process parameters for how to obtain defect-free equiatomic Co-Fe samples with relative density up to 99.8 ± 0.05% via LPBF.
- Detailed SEM-EBSD mapping on the AF and thermally post-processed states revealed that microstructure varied greatly after every heat treatment. The aforementioned microstructural investigation was linked with the complete quasi-static soft magnetic characterisation of all the states. Some of the heating profiles investigated produced undesirable soft magnetic responses and unconventional bimodal microstructures.
- Further investigation utilising neutron diffraction revealed that the AF state possessed a mainly a BCC disordered structure due to the high cooling rates of the LPBF process that is magnetically undesirable due to small grain size, higher magneto-crystalline anisotropy and smaller lattice constant associated with the disordered condition [51]. HT3, and HT6 obtain a fully ordered B2 (CsCl) structure because of the slow controlled cooling after each heat treatment cycle.
- Single-step normalisation heat treatment HT3 at 1300 K for 2 h produced a promising microstructure but again led to a degree of bimodality in the grain size distribution and hence sub-optimal soft magnetic performance. HT6 heat treatment with a normalisation step at 1300 K for 2 h followed by a 4 h primary heat treatment at 1123 K, achieved the best soft magnetic properties, comparable to the original equiatomic Co-Fe study [10] research work, and superior to that of HIPERCO® 50 A [49] and VACOFLUX 50 [50] commercial grades. The empirical equation from [54] has shown that HT3 and HT6 follow the trend of H_c vs D^{-1} similarly to the CM Co-Fe alloys.

The material investigated in this study demonstrated excellent soft magnetic properties and it is well known that has also a high Curie temperature [1]. This opens the road for the development of complex electromagnetic core geometries, for low and high temperature applications where sophisticated geometrical component design offers critical advantages and the employment of a laminates are not desirable due to structural integrity constrains.

CRediT authorship contribution statement

Konstantinos A. Liogas: Writing – original draft, Visualization, Validation, Software, Methodology, Investigation, Formal analysis, Data curation, Conceptualization. **Kwang Boon Lau:** Software, Methodology, Investigation. **Zifan Wang**: Methodology, Investigation, Formal analysis. **David N. Brown**: Writing – review & editing, Validation, Resources, Methodology, Investigation. **Efhymios Polatidis**: Visualization, Software, Methodology. **Pei Wang**: Writing – review & editing, Supervision, Resources, Project administration, Methodology, Investigation, Funding acquisition, Formal analysis, Conceptualization. **Alexander M. Korsunsky**: Writing – review & editing, Visualization, Validation, Supervision, Resources, Methodology, Investigation, Formal analysis, Data curation, Conceptualization.

Declaration of Competing Interest

The authors declare that they have no known competing financial interests or personal relationships that could have appeared to influence the work reported in this paper.

Data Availability

Data will be made available on request.

Acknowledgments

This work was supported by UK Engineering and Physical Sciences Research Council (EPSRC) through grant EP/V007785/1 "Rich Nonlinear Tomography for advanced materials" and the AME (IRG) Thematic Grant Call on Cleaner Manufacturing, grant No. A20E7c0109, in Agency for Science, Technology and Research in Singapore. The authors gratefully acknowledge the technical support for TEM sample preparation using FIB from Ms. Teo Siew Lang, sample polishing by Mr. Wei Hock The. We acknowledge the Paul Scherrer Institute, Villigen, Switzerland for the provision of neutron beamtime at the instrument POLDI of the SINQ under the proposal number 20211216.

References

[1] L. Li, J.Appl. Phys. 79 (1996) 4578.
[2] R.E. Quigley, Proc. IEEE Appl. Power Electron. Conf. 'More Electr. Aircr. (1993) 906–911.
[3] S.E. McKinlay, N. Fussing, R. Sinclair, M. Doerner, IEEE Trans. Magn. 32 (1996) 3587.
[4] T. Nishizawa, K. Ishida, Met. Progr 57 (1986).
[5] R.S. Sundar, S.C. Deevi, Soft magnetic FeCo alloys: alloy development, processing, and properties, Int. Mater. Rev. 50 (3) (2005) 157–192, https://doi.org/10.1179/174328005×14339.
[6] A. Preuss: 'Magnetic properties of Fe–Co alloys at different temperatures', dissertation, University of Zurich, 1912.
[7] P. Weiss, Trans. Faraday Soc. 8 (1912) 149–156.
[8] W.C. Ellis, Rensselaer Polytech. Inst. Bull. Eng. Sci. Ser. 16 (1927) 1–57.
[9] G.W. Elmen: U.S. Patent 1 739 752, 1929.
[10] G.W. Elmen, Magnetic alloys of iron, nickel, and cobalt, Bell Syst. Tech. J. 15 (1) (1936) 113–135, https://doi.org/10.1002/j.1538-7305.1936.tb00721.x.
[11] T. Sourmail, Near equiatomic FeCo alloys: constitution, mechanical and magnetic properties, Prog. Mater. Sci. 50 (7) (2005) 816–880, https://doi.org/10.1016/j.pmatsci.2005.04.001.
[12] E.P. George, A.N. Gubbi, I. Baker, L. Robertson, Mechanical properties of soft magnetic FeCo alloys, Mater. Sci. Eng. A 329 (2002) 325–333.
[13] A.R. de Oliveira, et al., Investigation of the build orientation effect on magnetic properties and Barkhausen noise of additively manufactured maraging steel 300, Addit. Manuf. 38 (2021), 101827, https://doi.org/10.1016/j.addma.2020.101827.
[14] A.B. Kustas, D.F. Susan, K.L. Johnson, S.R. Whetten, M.A. Rodriguez, D.J. Dagel, J. R. Michael, D.M. Keicher, N. Argibay, Characterization of the Fe-Co-1.5V soft ferromagnetic alloy processed by laser engineered net shaping (LENS), Addit. Manuf. 21 (2018) 41–52, https://doi.org/10.1016/j.addma.2018.02.006.
[15] S. Li, K.B. Lau, D. Wuu, F. Wei, M. Lin, A. Cheong, P. Wang, C.C. Tan, U. Ramamurty, 3D printing of ductile equiatomic Fe-Co alloy for soft magnetic applications, Addit. Manuf. 47 (2021), 102291, https://doi.org/10.1016/j.addma.2021.102291.
[16] W. Everhart, J. Newkirk, Grain size effects in selective laser melted Fe-Co-2V, Appl. Sci. 9 (18) (2019) 3701, https://doi.org/10.3390/app9183701.
[17] M.S.Y. Nartu, et al., Omega versus alpha precipitation mediated by process parameters in additively manufactured high strength TI–1Al–8V–5fe alloy and its impact on mechanical properties, Mater. Sci. Eng.: A 821 (2021), 141627, https://doi.org/10.1016/j.msea.2021.141627.
[18] J. Zou, et al., Controlling the grain orientation during laser powder bed fusion to tailor the magnetic characteristics in a Ni-FE based soft magnet, Acta Mater. 158 (2018) 230–238, https://doi.org/10.1016/j.actamat.2018.07.064.
[19] R.M. Bozorth: 'Ferromagnetism'; 1951, D. Van Nostrand Co. Inc.
[20] M.S.Y. Nartu, et al., Reducing coercivity by chemical ordering in additively manufactured soft magnetic Fe–Co (Hiperco) alloys, J. Alloy. Compd. 861 (2021), 157998, https://doi.org/10.1016/j.jallcom.2020.157998.
[21] G. Chin, J. Wernick, Chapter 2 Soft magnetic metallic materials. Handbook of Ferromagnetic Materials, Elsevier B.V., 1980, pp. 55–188.
[22] R.H. Yu, S. Basu, L. Ren, Y. Zhang, A. Parvizi-Majidi, K.M. Unruh, J.Q. Xiao, High temperature soft magnetic materials: FeCo alloys and composites, IEEE Trans. Magn. 36 (2000) 3388e3393.
[23] R.V. Major, C.M. Orrock, High saturation ternary cobalt-iron basalt alloys, IEEE Trans. Magn. 24 (1988) 1856e1858, https://doi.org/10.1109/20.11625.
[24] J.M. MacLaren, T.C. Schulthess, W.H. Butler, R. Sutton, M. McHenry, Electronic structure, exchange interactions, and Curie temperature of FeCo, J. Appl. Phys. 85 (1999) 4833e4835.
[25] M.F. Collins, J.B. Forsyth, The magnetic moment distribution in some transition metal alloys, Philos. Mag. A 8 (1963) 401e410.
[26] A.W. Smith, R.D. Rawlings, A neutron diffraction study of ordering in an ironecobalte1.8% vanadium alloy, Phys. Status Solidi 34 (1976) 117e123.
[27] C.-W. Chen, Magnetism and metallurgy of soft magnetic materials, Cour. Corp. vol. 15 (2013).
[28] G. Herzer, Grain size dependence of coercivity and permeability in nanocrystalline ferromagnets, IEEE Trans. Magn. 26 (5) (1990) 1397–1402, https://doi.org/10.1109/20.104389.
[29] R. Alben, J.J. Backer, M.C. Chi, J. Appl. Phys. 49 (1978), 1653.
[30] G. Herzer, I.E.E.E.Trans. Magn. 25 (1989) 3327.
[31] G. Herzer, Scr. Metal. Mater. 33 (1995) 1741.
[32] G. Herzer, J.Magn Magn, Mater 294 (2005) 99.
[33] D. Xue, et al., Effects of grain size distribution on coercivity and permeability of Ferromagnets, J. Magn. Magn. Mater. 320 (8) (2008) 1541–1543, https://doi.org/10.1016/j.jmmm.2008.01.004.
[34] A. A801, Standard Specification for Wrought Iron-Cobalt High Magnetic Saturation Alloys UNS, 1999. https://doi.org/10.1520/A0801–14.2.
[35] Specification for wrought iron-cobalt high magnetic saturation alloys (UNS R30005 and K92650)" (no date). Available at: https://doi.org/10.1520/a0801–21.
[36] F. Bachmann, R. Hielscher, H. Schaeben, Texture Analysis with MTEX–Free and Open Source Software Toolbox, Trans Tech Publications, 2010, pp. 63–68.
[37] O. Arnold, J.C. Bilheux, J.M. Borreguero, A. Buts, S.I. Campbell, L. Chapon, et al., Mantidddata analysis and visualization package for neutron scattering and m SR experiments, Nucl. Instrum. Methods Phys. Res. Sect. A Accel. Spectrometers Detect Assoc. Equip. 764 (2014) 156e66, https://doi.org/10.1016/j.nima.2014.07.029.
[38] F. Fiorillo, Measurements of magnetic materials, Metrologia 47 (2) (2010), https://doi.org/10.1088/0026-1394/47/2/s11.
[39] ASTM A773, Standard Test Method for dc Magnetic Properties of Materials Using Ring and Permeameter Procedures with dc Electronic, 01, ASTM, 2015, pp. 1–10, https://doi.org/10.1520/A0773.
[40] ASTM A977, 1997 Edition, October 10, 1997 - Standard Test Method for Magnetic Properties of High-Coercivity Permanent Magnet Materials Using Hysteresigrapghs, (Accessed: February 01, 2023).
[41] Magnet-physik dr. Steingroever GmbH (no date). Available at: https://www.magnetphysik.de/upload/18657949-Permagraph-L-e-3117.pdf (Accessed: February 01, 2023).
[42] L. Thijs, et al., A study of the microstructural evolution during selective laser melting of ti–6al–4v, Acta Mater. 58 (9) (2010) 3303–3312, https://doi.org/10.1016/j.actamat.2010.02.004.
[43] T. DebRoy, et al., Additive manufacturing of metallic components – process, structure and properties, Prog. Mater. Sci. 92 (2018) 112–224, https://doi.org/10.1016/j.pmatsci.2017.10.001.
[44] J. Dennis, P.S. Bate, F.J. Humphreys, Abnormal grain growth in al–3.5cu, Acta Mater. 57 (15) (2009) 4539–4547, https://doi.org/10.1016/j.actamat.2009.06.018.
[45] J. Li, et al., Selective abnormal growth behavior of Goss grains in magnetostrictive Fe-Ga alloy sheets, Mater. Trans. 57 (12) (2016) 2083–2088, https://doi.org/10.2320/matertrans.m2016152.
[46] D.W. Clegg, R.A. Buckley, The disorder → order transformation in iron–cobalt-based alloys, Met. Sci. J. 7 (1973) 48–54, https://doi.org/10.1179/030634573790445541.
[47] J.P. Eymery, P. Grosbras, P. Moine, Ordering kinetics of various Fe-Co alloys, Phys. Status Solidi (a) 21 (2) (1974) 517–528, https://doi.org/10.1002/pssa.2210210216.
[48] A.W. Smith, R.D. Rawlings, A neutron diffraction study of ordering in an iron–cobalt–1.8% vanadium alloy, Phys. Status Solidi (a) 34 (1) (1976) 117–123, https://doi.org/10.1002/pssa.2210340109.
[49] Carpenter Technology (2020), "HIPERCO® 50A", available at: https://f.hubspotusercontent20.net/hubfs/7407327/carpenter_electrification/Resources/Datasheets/Hiperco_50A_Alloy_(E199).pdf (accessed 01 September 2022).
[50] VACUUMSCHMELZE (2021), "Soft magnetic cobalt-iron alloys", available at: www.vacuumschmelze.de/fileadmin/Medienbibliothek_2010/Downloads/HT/Soft_Magnetic_CoFe_Alloys_05_2016.pdf (accessed 01 September 2022).

[51] R.H. Yu, et al., Pinning effect of the grain boundaries on magnetic domain wall in FECO-based magnetic alloys, J. Appl. Phys. 85 (9) (1999) 6655–6659, https://doi.org/10.1063/1.370175.
[52] C. Gan, J. Zhu, Study on the rolling process of 1j22 soft magnetic alloy, Mater. Sci. Forum 745–746 (2013) 119–125, https://doi.org/10.4028/www.scientific.net/msf.745-746.119.
[53] T. Ochirkhuyag, S.C. Hong, D. Odkhuu, Enhancing magnetic anisotropy and stability of α″-fe16N2 phase by CO and V co-substitution, AIP Adv. 11 (1) (2021), 015227, https://doi.org/10.1063/9.0000068.
[54] T. Sourmail, Evolution of strength and coercivity during annealing of Feco based alloys, Scr. Mater. 51 (6) (2004) 589–591, https://doi.org/10.1016/j.scriptamat.2004.05.028.
[55] L. Néel, Bases d'une nouvelle théorie générale du champ coercitif, Ann. Univ. Grenoble 22 (1946) 299–343.
[56] F. Pfeifer, C. Radeloff, Soft magnetic ni-fe and Co-Fe alloys - some physical and metallurgical aspects, J. Magn. Magn. Mater. 19 (1–3) (1980) 190–207, https://doi.org/10.1016/0304-8853(80)90592-2.
[57] Orrock C.M.. PhD thesis, London University, 1986.